2024 IEEE/RSJ International Conference on Intelligent Robots and Systems (IROS)
October 14-18, 2024. Abu Dhabi, UAE

Underwater Hyperspectral Imaging for Measuring Seafloor Reflectance

Hongjie Zhang*,[1], Gideon Billings[1], Jackson Shields[1], Stefan Williams[1]

***Abstract*— A known challenge for computer vision methods applied to the underwater domain is that nonlinear attenuation of light in underwater environments distorts the color signal in captured imagery, resulting in inconsistent color and contrast at varying distances to an imaged target. While surface reflectance can provide a useful cue for classifying imagery of the seafloor by object or substrate types, color inconsistency makes robust classification challenging. We introduce a method that leverages hyperspectral imagery with an underwater light formation model and structure from motion to estimate the intrinsic optical properties of the underwater environment and correct seafloor reflectance estimates from radiance measurements. We show that our method enables consistent surface reflectance estimates under both artificial and ambient lighting conditions and is readily integrated on small underwater vehicle platforms, such as a BlueROV.**

***Index Terms*— Marine Robotics, Computer Vision for Automation, Environment Monitoring and Management, Mapping**

I. Introduction

Underwater ecosystems, such as coral reefs, kelp forests, and seagrass beds, are vital for supporting a rich diversity of marine life. The conservation of these underwater habitats is of great importance due to their significant social and economic value [1]. Yet, these precious habitats are increasingly threatened by pollution and rising ocean temperatures. Monitoring these habitats is critical to understanding their environmental stresses and ensuring their health and sustainability. Habitat monitoring can be conducted through both above-water and underwater methods [2]. Above-water monitoring employs remote sensing systems on aircraft or satellites, usually utilizing hyperspectral devices to capture high spectral resolution data [2]. This approach allows for the efficient coverage of large areas, making it ideal for broad-scale monitoring efforts. However, remote sensing usually has low spatial resolution and is limited to shallow water environments (generally down to 20 meters deep) due to the reliance on natural ambient light, which is attenuated and scattered with depth. On the other hand, underwater monitoring with platforms such as Autonomous Underwater Vehicles (AUVs), Remotely Operated Vehicles (ROVs) [3], or towed camera systems [4], offer higher spatial resolution. Yet, these systems are typically equipped with monochrome or RGB cameras rather than hyperspectral sensors because of the challenges associated with deploying these sensors subsea. One of the major challenges is the nonlinear attenuation and scattering effects of water on light, which distorts the spectral response and hinders accurate hyperspectral analysis.

[1]with the Australian Centre for Field Robotics, the University of Sydney, NSW, Australia
* primary contact: hzha5857@uni.sydney.edu.au

The effectiveness of hyperspectral imaging (HSI) for classification and analysis hinges on its utility for distinguishing materials based on their distinct reflectance signatures [5]. Under normal conditions above water, reflectance can be readily derived from radiance measurements and knowledge of the natural light spectrum in the surveyed area, as the atmosphere's attenuation effect on the visible light spectrum is minimal. However, this is not the case in underwater environments, where the inherent attenuation effects of the optical medium introduce a significant challenge to underwater HSI. Attenuation effects cause the intensity of the measured radiance signal to diminish in a wavelength dependent manner with a nonlinear dependence on the distance to the imaged target, leading to spectrum distortions and a loss of contrastive detail [6]. Additionally, the variability in water turbidity, caused by suspended organic particulates, across different environments exacerbates the inconsistency of attenuation rates, hindering the predictability and standardization of imaging processes [7]. These challenges impede the accurate estimation of underwater surface reflectance from HSI, limiting its direct application for seafloor classification. Therefore, the primary objective of this work is to develop an in-situ method for accurately correcting the true reflectance of underwater surfaces from HSI measured radiance signals by estimating and compensating for the wavelength dependent intrinsic optical properties of water.

In this work, we make the following contributions and evaluations:

- A novel method for estimating underwater surface reflectance from hyperspectral imaging measurements, leveraging a simplified underwater light formation model and structure from motion (SfM).
- The formulation of our method under two lighting scenarios, where the light source is fixed relative to the camera, or the scene is illuminated from a constant ambient light source external to the camera rig.
- Quantitative assessment of our proposed method in a controlled laboratory tank setup, under both fixed artificial lighting and ambient lighting scenarios.
- Assessment of the proposed method in a natural harbour environment, with the imaging system deployed on a BlueROV2, under ambient sunlight conditions.

A key strength of our proposed method lies in its independence from prior assumptions about the reflectance properties of underwater surfaces or the specific water type, such as Jerlov classifications, thereby eliminating the need for predefined parameter bounds in the optimization. The experimental results demonstrate the utility of our method for

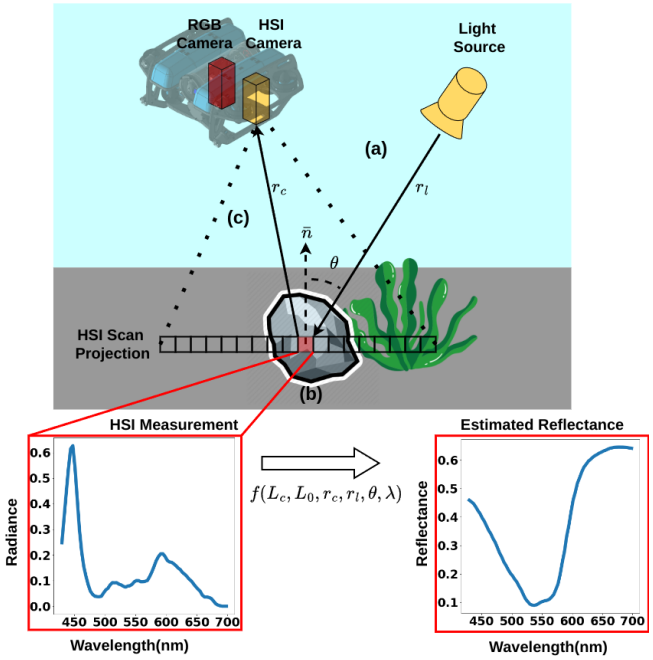

Fig. 1: Underwater light formation model, depicted across three stages: (a) Light travels a distance of r_l from the source to the target surface, experiencing water attenuation. (b) Assuming a Lambertian surface, light reaches the surface at an incident angle of θ and is reflected according to the surface reflectance. (c) The reflected light traverses a distance of r_c to the camera, undergoing further attenuation. The HSI camera is integrated with an RGB camera that provides geometric information of the scene through SfM. The registration of hyperspectral measurements with scene geometry enables estimation of the surface reflectance spectrum.

accurately estimating underwater surface reflectance under varying lighting conditions.

II. Related Work

The Radiative Transfer Equation (RTE) is the fundamental model that describes light propagation through a medium, such as water, air, or plant canopies [8]. In underwater hyperspectral imaging, the RTE relates the sensor radiance measurement to the inherent optical properties (IOPs) of the water (i.e., absorption and scattering coefficients), the light source and scene geometries, the surface reflectance function, and other properties of the scene [9]. Various solutions or approximations of the RTE have been proposed, including numerical [10], empirical [11], and semi-analytical (SA) [12] approaches. SA approaches have been largely adopted in recent research on underwater image formation for their computational tractability and accurate approximation for the underwater medium. The Hyperspectral Optimization Processing Exemplar (HOPE) model [12] is a well-known SA model solving the RTE for shallow water hyperspectral remote sensing. The HOPE model parameterizes water column absorption, backscattering coefficients, and bottom reflectance as scalar variables and utilizes spectral optimization to estimate IOPs and seafloor depth. Subsequent SA models for shallow water hyperspectral remote sensing such as BRUCE [13], SAMBUCA [14], and BOMBER [15] adopt a similar methodology. These SA methods have demonstrated their effectiveness in estimating IOPs and seafloor depth when provided with prior knowledge of the spectral shape of the bottom reflectance. While these models provide a framework for solving underwater IOPs, the seafloor reflectance is often unknown, limiting the utility of these methods for general IOP estimation.

Recent works have built on these remote sensing models and combined them with SfM techniques to concurrently estimate IOPs and seafloor reflectance in-situ [16], [6]. In [16], a new SA model was proposed, based on the works of [17], [18], [19], for estimating the IOPs and surface reflectance of the seafloor using underwater RGB images. The estimated IOPs and surface reflectance are used for image color correction. Given that the simultaneous estimation of IOPs and bottom reflectance is an underdetermined problem, this work proposed a multiple point optimization strategy, using observations from different angles, depths, and locations to minimize uncertainty in optimization. Most similar and concurrent to our work, the study in [20] integrates the light propagation models from the HOPE model [12] and the Jaffe–McGlamery model [21], [17], along with the SfM and multipoint optimization strategies from [16], to estimate IOPs and bottom reflectance from underwater hyperspectral measurements. Their approach is developed for artificial light sources, and they parameterise the optimization of the IOPs. Our proposed method adopts a similar, though more simplified SA model, from [16], and we directly optimize the IOPs without parameterization, making no prior assumptions about the IOP spectral shape. In addition, the focus of our work is on accurate estimation of the seafloor reflectance, and we propose a method that can be applied under both artificial and ambient light conditions.

Also related to our work, the study in [6] introduced a novel approach for estimating IOPs and seafloor reflectance from underwater, single-point, spectrometer measurements, utilizing three different sensors. The setup involved positioning one spectrometer on a surface vessel and two on an underwater platform, with one aimed upwards and one downwards. This setup allows for IOP determination by applying a SA model to measurements from the upward-looking spectrometer on the vehicle and the downward-looking spectrometer on the surface vessel. The IOPs obtained are then used to evaluate seafloor reflectance with the downward-looking spectrometer. In contrast, our method uses a low-cost, push-broom style HSI camera that provides greater spacial coverage than the single point spectrometers used in [6] and requires only one hyperspectral camera on the underwater platform, offering a solution that is readily integrated on small mobile vehicles for deployment completely in-situ.

III. Method

This section presents our method for estimating the intrinsic, wavelength-dependent water attenuation coefficient

and corrected surface reflectance spectrums from hyperspectral imaging (HSI) measurements. We begin by introducing the underwater light propagation model underlying our method. Subsequently, we present our optimization formulations for solving for the attenuation coefficient and surface reflectances under two distinct scenarios: one with artificial light sources and the other with ambient light.

A. Underwater Light Propagation Model

As depicted in Figure 1, the radiance signal captured by an HSI sensor can be modelled as a sequence of three light propagation stages: (a) light transmission through the water column from a source to the target surface, (b) light reflection at the target surface, and (c) transmission of the reflected light through the water column to the sensor. Our method uses a simplified underwater light transmission model that combines the light signal loss from absorption and scattering into a single, wavelength-dependent attenuation factor, $b(\lambda)$. The light signal attenuation is given by Beer-Lambert's Law [22] as

$$L_d(\lambda) = L_0(\lambda)e^{-b(\lambda)d} \tag{1}$$

where $L_0(\lambda)$ is the initial radiance for wavelength λ and $L_d(\lambda)$ denotes the radiance signal at distance d from the source.

The transmission of a light source to the target surface is modelled differently according to whether the light source is ambient or artificial, which we address in the following sections. Given an irradiance signal from some light source incident on the target surface, we model the Bidirectional Reflectance Distribution Function (BRDF) as a Lambertian surface [16], where it is assumed the reflected light radiance, $L_s(\lambda)$, is uniform from any surface viewing direction. The transmission of the reflected radiance received by the HSI sensor is then given simply as

$$L_c(\lambda) = L_s(\lambda)e^{-b(\lambda)r_c}, \tag{2}$$

where $L_c(\lambda)$ is the radiance signal measured by the HSI sensor and r_c is the distance between the sensor and the target surface.

B. Reflectance Model Under Artificial Light

In the case of artificial lighting, we assume that artificial illumination is the sole light source irradiating the surface imaged by the HSI camera. This scenario is relevant when operating in deep water or in very low ambient light conditions, such as at night time.

1) Light source model: In our approach, we model artificial light sources, such as dive lights, to emit a spherical cone of light with isotropic radiance. Given a light source with power in flux, Φ, and underwater beam spread angle, θ_l, the spectral irradiance on a surface at distance r_l from the source without attenuation effects is given by the inverse square law as [23]:

$$E_0(\lambda, r_l) = \frac{\Phi(\lambda)}{\pi \times (r_l \times \tan\frac{\theta_l}{2})^2} \tag{3}$$

Combining this light spread function with the underwater transmission model given in Equation 1, the incident irradiance on the underwater surface is given as

$$E_s(\lambda) = E_0(\lambda, r_l)e^{-b(\lambda)r_l} \tag{4}$$

Given the Lambertian model for the surface BRDF, the reflected radiance signal from any viewing direction is given as [24]

$$L_s(\lambda) = \frac{a(\lambda)E_s(\lambda)\cos(\theta)}{\pi}, \tag{5}$$

where $a(\lambda)$ is the surface reflectance at wavelength λ and θ is the angle between the surface normal and the incoming light direction. For multiple light sources, the total radiance signal reflected from the surface can be calculated by computing the individual signals for each light source and summing them.

2) Scene geometry: Modeling the reflectance signal requires knowing the surface normal vector at the irradiated point and the angle of the incoming irradiation with respect to the surface normal. We reconstruct a surface mesh of the scene using SfM with an RGB camera that is fixed and extrinsically calibrated to the HSI camera. For the experiments in this work, we use the Agisoft Metashape software to construct the 3D meshes, and we also place AprilTags in the surveyed scene and use TagSLAM [25] to estimate the camera rig pose for each frame. We note that the use of TagSLAM is a choice of convenience for this work because we use only a monocular RGB camera for the SfM, which does not provide scale consistency. The optimized poses from SfM could be used directly if a stereo-based or other method that provides true metric scaling is used.

The extrinsic calibration between the HSI and RGB cameras follows the approach outlined in [26] and [27], and the extrinsic calibration between the light source and RGB camera are manually measured. Given these calibrations, the HSI camera can be accurately projected into the scene 3D mesh reconstruction. For each pixel of the HSI camera, this projection yields the range, r_c, to the imaged area on the surface. Additionally, the imaged area for each pixel on the surface can be raytraced back to the co-registered light source to determine the range, r_l, from the light source to the surface and the incident angle, θ, of the light with respect to the surface normal.

3) Optimization formulation: Given the HSI measurements and 3D mesh of the scene, an optimization is formulated to recover the water attenuation coefficient and the surface reflectances. The 3D mesh is divided into unit triangular regions, each presumed in the optimization to contain only one material. A set of M triangular regions, representative of the different materials in the scene, is randomly selected. For each wavelength λ, the optimization targets the estimation of the surface reflectance, $a(\lambda)$ of each chosen region and the water attenuation, $b(\lambda)$, expressed in

an array of optimized parameters as follows:

$$[b(\lambda), a_1(\lambda), \dots a_M(\lambda)] \tag{6}$$

The optimization strategy requires multiple HSI measurements from the same triangular region. For each wavelength, the measurements are collected into an array as follows,

$$\left[L_1^1(\lambda), \dots, L_1^{N_1}(\lambda), \dots, L_M^1(\lambda), \dots, L_M^{N_M}(\lambda)\right], \tag{7}$$

where L_i^j denotes the j^{th} radiance measurement of the i^{th} triangular region. Given the assumption that these triangular regions are relatively small compared to their distance from the HSI camera, any HSI pixels from the same scan that project onto the same triangular region are averaged across wavelengths.

Combining Equations 2, 3, 4, and 5, the function that relates the optimization parameters to the radiance measurements is given as

$$\mathbf{L} = \frac{a_i(\lambda)\Phi(\lambda)\cos(\theta_{l_i}^j)e^{-b(\lambda)(r_{c_i}^j + r_{l_i}^j)}}{(\pi \times r_{l_i}^j \times \tan\frac{\theta_{\text{beam}}}{2})^2} \tag{8}$$

We formulate the objective function to be minimized over the radiance measurements as

$$\sum_{i=1}^{M}\sum_{j=1}^{N_M}(L_i^j(\lambda) - \mathbf{L}(b, a_i, r_{c_i}^j, \Phi, \theta_{\text{beam}}, r_{l_i}^j, \theta_{l_i}^j, \lambda))^2 \tag{9}$$

The optimization of the attenuation coefficient and surface reflectance is subject to absolute physical bound constraints. The attenuation coefficient cannot be less than zero, as it is physically impossible for light to be amplified during its underwater propagation. In addition, the surface reflectance, being a proportion, must be confined within the range 0 to 1. These constraints necessitate a tailored optimization approach, leading to our use of the Trust Region Reflective (TRR) algorithm [28]. The TRR algorithm dynamically adjusts a trust region to adhere to the imposed bounds, enhancing robustness and efficiency [28]. Moreover, TRR is engineered to inherently avoid common pitfalls, such as converging to infeasible points, making it suited for tasks requiring bounded optimization.

C. Reflectance Model Under Ambient Light

In the case of ambient lighting, we assume illumination of the seafloor is provided via a uniform, constant light source external to the vehicle. This scenario is most relevant to shallow water environments in sunny daytime conditions. The optimization problem is formulated as a two step problem, where first the attenuation coefficient is estimated under the constant illumination assumption, and then the normalized surface reflectance is recovered by applying the underwater light propagation model with a correction for the shape of the ambient light spectrum.

1) Ambient light model: Under constant and uniform ambient light conditions, let E_d denote the total downwelling plane irradiance just below the surface of the water, as defined in [29]. The radiance signal reflected from the seafloor and measured by the HSI is then given as

$$L(\lambda) = a(\lambda)E_d e^{-b(\lambda)(r_c+d)} \tag{10}$$

where d is the water depth, r_c is the distance from the HSI to the imaged point on the seafloor, $a(\lambda)$ is the surface reflectance, and $b(\lambda)$ is the attenuation coefficient. Given two HSI measurements of the same seafloor region from different imaging ranges, r_{c1} and r_{c2}, we can plug these two measurements into Eq. 10 and take their ratio to cancel the constant terms, leaving the following functional form that can be solved for the attenuation coefficient

$$\frac{L_1(\lambda)}{L_2(\lambda)} = e^{-b(\lambda)(r_{c1}-r_{c2})} \tag{11}$$

$$b(\lambda) = -\frac{\log(\frac{L_1(\lambda)}{L_2(\lambda)})}{(r_{c1}-r_{c2})}. \tag{12}$$

Plugging the estimation for $b(\lambda)$ back into Eq. 10 gives a solution for $a(\lambda)E_d$, the surface reflectance multiplied by the unattenuated downwelling irradiance spectrum. While accurately modeling the absolute downwelling irradiance is a complicated problem that must account for the azimuth angle of the light source on the air-water interface, the shape of the unattenuated ambient spectrum is readily obtained by taking an HSI measurement of a target with known reflectance, illuminated by the ambient source in air. In this work, we simplify the ambient light case by seeking only to estimate the normalized shape of the surface reflectance spectrum, which is still a strong indicator of material visual properties. Let the absolute downwelling irradiance be given as $E_d = P\bar{E}_d$, where $\bar{E}_d$ is the normalized irradiance spectrum and P is a constant multiplier. Given the HSI measurement of $\bar{E}_d$ at the surface, we can divide this into the estimate of $a(\lambda)E_d$ to recover $Pa(\lambda)$, where the reflectance spectrum is estimated to a constant multiplier. This estimate can be normalized in turn to obtain $\bar{a}(\lambda)$, the shape of the surface reflectance spectrum.

2) Optimization formulation: In the ambient light case, the parameter to optimize is simply the attenuation coefficient, $b(\lambda)$. The objective function takes a similar form to the artificial light case, but relates the ratio of two HSI measurements of the same region, captured from different ranges. The objective function is formulated as follows

$$\sum_{i=1}^{N}(\frac{L_1^i(\lambda)}{L_2^i(\lambda)} - \bar{\mathbf{L}}(b, r_{c1}^i, r_{c2}^i, \lambda))^2 \tag{13}$$

where $L_1^i(\lambda)$ and $L_2^i(\lambda)$ are the i^{th} measurements captured from the same triangular region at ranges r_{c1}^i and r_{c2}^i respectively, and $\bar{\mathbf{L}}$ is a functional map to Equation 11. The Trust Region Reflective algorithm [28] is also used to optimize the objective function in this scenario.

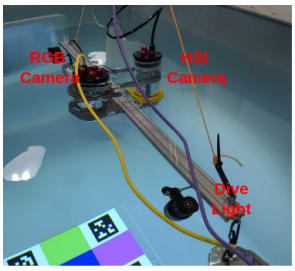

(a) Camera rig used in tank experiment

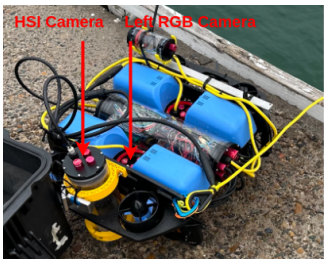

(b) Blue ROV2 used in field experiment

Fig. 2: Hardware setups for experiments.

IV. Experimental Setup

The hyperspectral camera used in this work is the OpenHSI camera [30], which is a line scan hyperspectral imaging device. Fig. 2 shows the hardware setups for the tank and field experiments. The normalized spectrum of the different light sources used in the experiments are plotted in Fig. 4.

A. Laboratory Setup

In the laboratory tests, the HSI and RGB cameras were rigidly fixed to each other on a rig. A experiment was conducted with an I-Torch Venom 50 dive light rigidly fixed to the camera rig at an offset of 0.475 m and angled towards the cameras at 30° relative to the z-axis of the camera frames. The light had a measured power of 4115 Lumens and a manufacturer specified beam spread angle underwater of 100°.

An experiment was also conducted with a 1200 Lumen LED stand light positioned above the tank. Care was taken in the positioning of the stand light and during collection of the dataset to prevent shadowing of the imaged target by the camera rig.

A printed target was used (Fig. 3), featuring april tags in each corner and a pattern of five distinct colors. The ground truth reflectance of each color and the white regions of the target were measured with an ASD spectrometer.

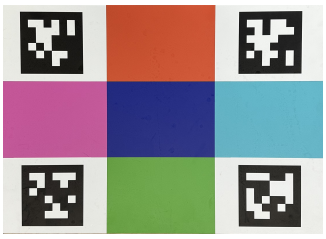

(a) Target board

(b) Field experiment

Fig. 3: For evaluation, a target was used with 5 different color regions known reflectance spectrums (left image). The April Tags on the four corners were used to localize the camera relative to the target. The water quality at the field testing site in Sydney Harbour was highly turbid, as illustrated in the right RGB image captured at 2.8m above the seafloor, with the target sitting between patches of kelp and sand.

B. Field Setup

The ambient light model was further validated with field data collected at Chowder Bay, Sydney. For this test, an HSI camera was installed on a BlueROV 2 and co-registered with a downward facing RGB camera. The same color target used in the tank experiments was placed on the seafloor to serve as the test target, in order to evaluate consistency across tank and field experiments. As illustrated in fig. 3, the water quality at the field testing site in Sydney Harbour was highly turbid, representing a challenging real-world environment for underwater imaging.

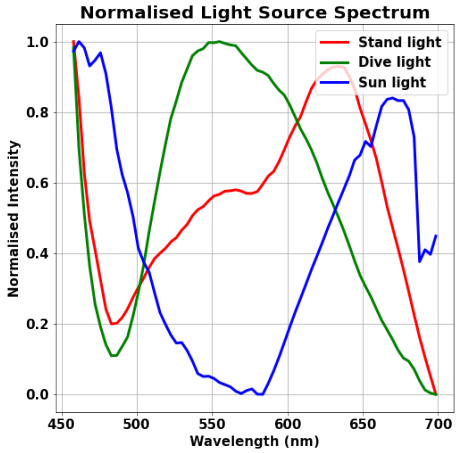

Fig. 4: The normalised spectrums of the source lights for the different experiments, measured with the HSI sensor. ”Stand light” is for the ambient light tank experiment, ”Dive light” is for the fixed light tank experiment, and ”Sun light” is for the field experiment.

V. Results

A. Tank experiment with fixed light

For the experiment conducted in a tank with the light source fixed to the camera rig, figure 5a shows the re-projection of HSI scans onto the 3D mesh reconstruction of the color target.

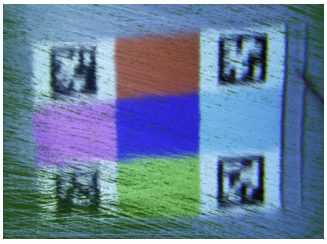

(a) Tank experiment

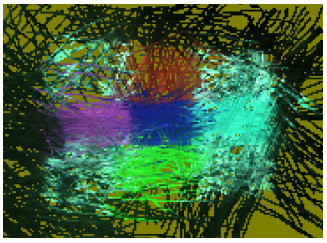

(b) Field experiment

Fig. 5: Visualization of the hyperspectral scan lines projected onto the 3D scene meshes constructed from co-registered RGB images for a tank experiment and the field experiment.

HSI measurements were collected at three depths, with ranges from the target of 1.5m, 1m, and 0.5m. Given the white region of the target provides the strongest reflection

across all wavelengths, we used measurements from the white region to optimize for the water attenuation coefficient. The white region was selected as it acts as a proxy for sand in the field setting, which is the most reflective natural surface and generally provides a strong reflectance across a wide spectrum band. We first estimated a reference attenuation coefficient for the tank water by optimizing over the HSI measurements of the white target regions with the reflectance spectrum of the white target fixed to the ground truth values in the optimization. Fig. 6 shows a plot of the estimated reference attenuation spectrum (green line). It is notable that the attenuation spectrum is higher than that for pure water, which is also plotted in the figure (purple dashed line). This difference is likely explained by the tank having regular chemical treatments for maintenance as well as being used regularly for rinsing vehicles after they have been deployed in the field, resulting in some amount of suspended particulates.

We then evaluated our full optimization approach by jointly optimizing the attenuation spectrum of the water and the reflectance spectrum of the white target, using HSI measurements from randomly selected triangular regions of the mesh that lay within the white regions. This estimated attenuation spectrum is also plotted (red line) in fig. 6. The estimated attenuation spectrum from this joint optimization closely matches the reference spectrum, demonstrating that our semi-analytical model for underwater light propagation and reflection well approximates the real environment.

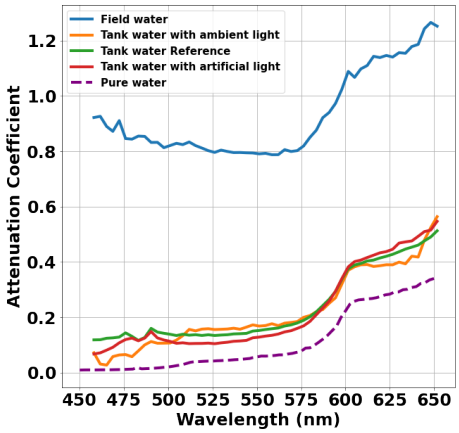

Fig. 6: Estimated water attenuation coefficients for the tank and field experiments. The pure water attenuation coefficient is extract from [31]

Given the optimized water attenuation coefficient spectrum from the white region measurements, we then fixed this coefficient in the optimization to estimate the reflectance of the different color regions, using HSI measurements from triangular regions of the 3D mesh that lied within each color. Figure 7 presents the reflectance estimations for the 5 different color regions of the target. Each sub-figure shows the average estimated reflectance (blue line) and the ground truth reflectance (red line). The estimates generally follow the ground truth values, with most estimates closely aligning with the ground truth. Notably, estimates for the blue regions exhibit lower reflectance than the ground truth beyond the 600nm wavelength, primarily due to the dive light's low power after 600nm (as shown in Figure 4) and the inherently low reflectance of blue regions at higher wavelengths. This leads to a poorly constrained optimization from small and potentially noisy radiance measurements for the blue region at these wavelengths, resulting, for this case, in the calculated reflectance being lower than the actual ground truth.

A limitation of the tank experiments was the shallow depth of the tank ($<$ 2m) and restricted size, which constrained the depth separation and viewing angles between measurement sets, making the resulting optimization sensitive to noise or inaccuracies in the model. Also, measurements taken too close to the target resulted in overexposure of the HSI and hot-spotting of the dive light, introducing an additional source of potential error.

Table I presents the average standard deviation of the estimated reflectance across wavelengths and the cosine similarity to the ground truth values for each color. The results indicate low average standard deviations for all colors. Cosine similarity measures the shape alignment between two lines, where a value of 1 indicates identical shapes. The high cosine similarities across all colors suggest that the estimated spectral shapes are very similar to their ground truth, and the estimation accuracy is consistent across the different colors.

TABLE I: Evaluation of the reflectance estimates from the tank experiment with a light source fixed to the camera rig. The Cosine Similarity score is with respect to the ground truth reflectance spectrums.

Color	Average Standard Deviation	Average Cosine Similarity
Red	0.0268	0.9988
Green	0.0188	0.9984
Blue	0.0200	0.9937
Cyan	0.0130	0.9912
Magenta	0.0328	0.9975

B. Tank and field experiments with ambient light

In the ambient light experiments, the absolute value of the attenuation coefficient is estimated, while the estimated reflectance spectrums are normalized.

For the experiment conducted in the tank with the external stand light, we optimized the attenuation coefficient on only measurements of the white region of the target board as a proxy to sand in the field setting. Fig. 6 shows a plot (orange line) of the estimated attenuation coefficient, which matches the reference spectrum closely.

For the experiment conducted in the field, we optimized the attenuation coefficient on measurements from sandy regions, which is plotted (blue line) in fig. 6. The high attenuation spectrum indicates strong turbidity with a green color tint in this harbour environment, which aligns with our visual observations of the water. The reprojection of the HSI scans in the 3D mesh reconstruction of the field data is shown in fig. 5b. The reprojections generally show the correct shape and color distribution of the target, but some blurring and inaccuracy is observed compared to the tank reprojections,

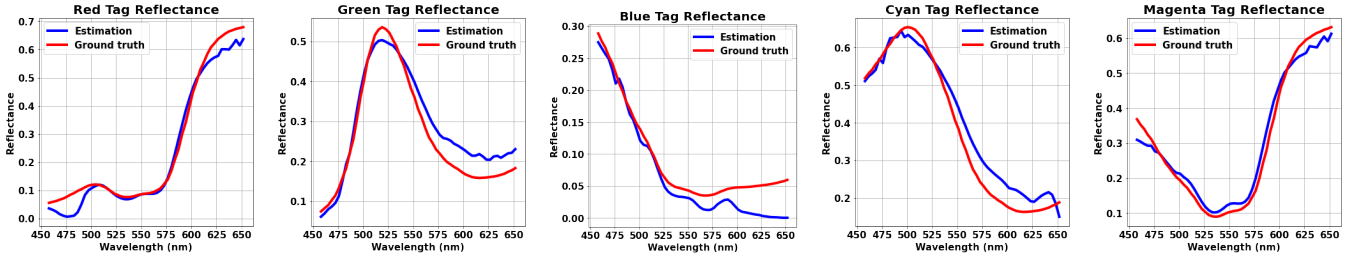

(a) Red (b) Green (c) Blue (d) Cyan (e) Magenta

Fig. 7: Reflectance estimates for the color targets for the tank experiment with an artificial light source fixed to the camera rig.

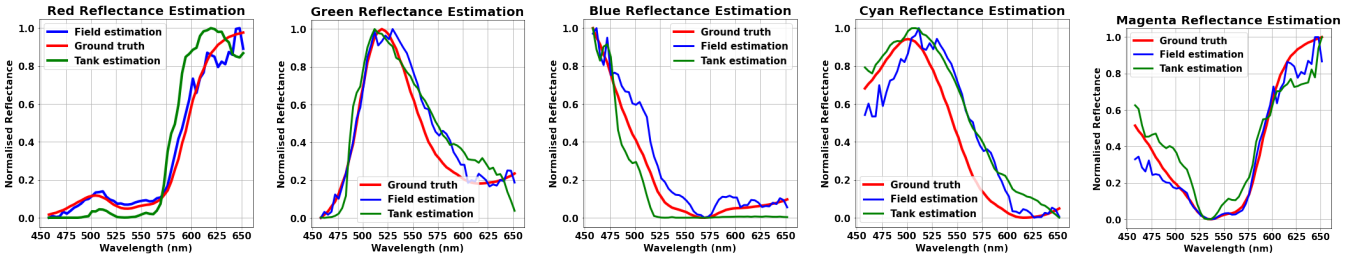

(a) Red (b) Blue (c) Green (d) Cyan (e) Magenta

Fig. 8: Reflectance estimates for the tank and field experiments under ambient light conditions.

resulting from the high water turbidity degrading the quality of the April Tag detections for pose estimation.

The normalized reflectances of the target colors were estimated using the optimized attenuation coefficient and correcting for the shape of the ambient light spectrum. The ambient light spectrum was estimated by taking in air HSI measurements of a white target with known reflectance and dividing the measured radiance from the target by the reflectance spectrum. Figure 8 presents the normalized reflectance estimates for each color of the target for both the tank (green line) and field (blue line) ambient lighting experiments, compared to the ground truth normalized reflectance spectrums (red line). In both cases, the estimates closely match the ground truth spectrums.

We note that the cyan reflectance estimations from both tank and field data show a spectral shift, where the peak reflectance of the estimations appear at a higher wavelength than the ground truth, and the estimated spectrum beyond 500nm is consistently higher than the ground truth. We analyzed this result further by estimating the cyan color target reflectance from in air HSI measurements under ambient light, while using a known white reflectance target to estimate the incident irradiance spectrum on the target. The resulting reflectance estimate showed a similar spectral shift to the underwater estimates, as plotted in fig. 9. We conjecture this spectral shift, most obvious in the cyan target, is likely due to a calibration error in the HSI sensor. However, the reflectance estimates from HSI measurements across tank and field experiments are self consistent.

A limitation of the ambient light case is the strong attenuation of higher wavelengths with depth, particularly in high turbidity such as the demonstrated harbour environment, which challenges the estimation of the attenuation and reflectance spectrums above 575nm when there is not enough light signal in these wavelengths for the optimization.

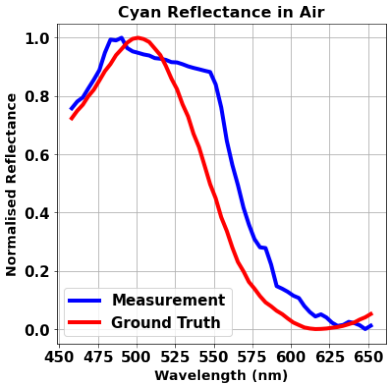

Fig. 9: Cyan reflectance derived from in air HSI measurements, showing a spectral shift compared to the ground truth, consistent with the underwater estimates.

VI. Conclusion

In this work, we introduce a semi-analytical model to estimate surface reflectance and water attenuation coefficients from underwater hyperspectral imaging. The method employs an RGB camera co-registered with an HSI sensor to reconstruct the scene geometry and enable accurate modeling of the HSI measurement formation process. The imaging system is readily integrated on small underwater vehicles, such as a BlueROV, and our proposed method for estimating surface reflectance spectrums can be applied with lighting carried onboard the vehicle or under ambient lighting conditions. The method requires no prior knowledge

of the seafloor environment or water characteristics, making it readily deployable to unexplored sites. We validated the model's accuracy and consistency in estimating surface reflectance through both laboratory and field experiments. These results motivate future work where we will explore the application of hyperspectral imaging to enhance underwater object and material classification over large-scale surveys. Future work will also address some of the current limitations of our approach by exploring the comparative performance of more complex underwater light formation models, such as the model proposed in [20], which separately considers absorption and backscattering. Also, adopting the parameterization process for water attenuation coefficient estimation, as suggested in [12], could constrain the estimation under low light conditions or reduce the number of required measurements to obtain an accurate estimate. Further, stereo-based SfM can replace TagSLAM in order to enable practical deployments over large survey areas. In addition, while this work assumed each hyperspectral pixel observed only one material, in reality, each pixel can often overlap multiple materials, resulting in a mixed spectral response. Future work could also explore spectral unmixing to improve reflectance estimates. Finally, our method relies on accurate SfM mesh reconstructions for triangulating hyperspectral projections. Feature poor environments or high turbidity could degrade the mesh reconstruction and the method performance. Future work could explore the integration of machine learning methods for SfM which may address some limitations of the conventional approaches.

REFERENCES

[1] C. Parliament, "Marine environment," May 2017.

[2] D. L. Bongiorno, M. Bryson, T. C. L. Bridge, D. G. Dansereau, and S. B. Williams, "Coregistered hyperspectral and stereo image seafloor mapping from an autonomous underwater vehicle," *Journal of field robotics*, vol. 35, no. 3, pp. 312–329, 2018.

[3] M. Dunbabin and L. Marques, "Robots for environmental monitoring: Significant advancements and applications," *IEEE Robotics & Automation Magazine*, vol. 19, no. 1, pp. 24–39, 2012.

[4] J. H. Carleton and T. J. Done, "Quantitative video sampling of coral reef benthos: Large-scale application," *Coral Reefs*, vol. 14, no. 1, p. 35–46, 1995.

[5] R. Smith, "Introduction to hyperspectral imaging from microimages."

[6] D. L. Bongiorno, M. Bryson, T. C. Bridge, D. G. Dansereau, and S. B. Williams, "Coregistered hyperspectral and stereo image seafloor mapping from an autonomous underwater vehicle," *Journal of Field Robotics*, vol. 35, no. 3, p. 312–329, 2017.

[7] D. Berman, D. Levy, S. Avidan, and T. Treibitz, "Underwater single image color restoration using haze-lines and a new quantitative dataset," *IEEE Transactions on Pattern Analysis and Machine Intelligence*, p. 1–1, 2020.

[8] W. L. Dunn and J. K. Shultis, "Chapter 7 - inverse monte carlo," in *Exploring Monte Carlo Methods (Second Edition)* (W. L. Dunn and J. K. Shultis, eds.), pp. 255–290, Elsevier, second edition ed., 2023.

[9] R. Garcia, Z. Lee, and E. Hochberg, "Hyperspectral shallow-water remote sensing with an enhanced benthic classifier," *Remote sensing (Basel, Switzerland)*, vol. 10, no. 1, pp. 147–, 2018.

[10] B. M. Herman and S. R. Browning, "A numerical solution to the equation of radiative transfer," *Journal of Atmospheric Sciences*, vol. 22, no. 5, pp. 559–566, 1965.

[11] H. Lv, Y. Wang, and Y. Shen, "An empirical and radiative transfer model based algorithm to remove thin clouds in visible bands," *Remote Sensing of Environment*, vol. 179, pp. 183–195, 2016.

[12] Z. Lee, K. L. Carder, C. D. Mobley, R. G. Steward, and J. S. Patch, "Hyperspectral remote sensing for shallow waters. 2. deriving bottom depths and water properties by optimization," *Applied Optics*, vol. 38, no. 18, pp. 3831–3843, 1999.

[13] W. M. Klonowski, P. R. Fearns, and M. J. Lynch, "Retrieving key benthic cover types and bathymetry from hyperspectral imagery," *Journal of Applied Remote Sensing*, vol. 1, no. 1, pp. 011505–0115021, 2007.

[14] K. Barott, J. Smith, E. Dinsdale, M. Hatay, S. Sandin, and F. Rohwer, "Hyperspectral and physiological analyses of coral-algal interactions," *PloS one*, vol. 4, no. 11, pp. e8043–e8043, 2009.

[15] C. Giardino, G. Candiani, M. Bresciani, Z. Lee, S. Gagliano, and M. Pepe, "Bomber: A tool for estimating water quality and bottom properties from remote sensing images," *Computers & geosciences*, vol. 45, pp. 313–318, 2012.

[16] M. Bryson, M. Johnson-Roberson, O. Pizarro, and S. B. Williams, "True color correction of autonomous underwater vehicle imagery," *Journal of Field Robotics*, vol. 33, no. 6, p. 853–874, 2015.

[17] J. Jaffe, "Computer modeling and the design of optimal underwater imaging systems," *IEEE journal of oceanic engineering*, vol. 15, no. 2, pp. 101–111, 1990.

[18] S. J. Kim and M. Pollefeys, "Robust radiometric calibration and vignetting correction," *IEEE transactions on pattern analysis and machine intelligence*, vol. 30, no. 4, pp. 562–576, 2008.

[19] M. Grossberg and S. Nayar, "Modeling the space of camera response functions," *IEEE transactions on pattern analysis and machine intelligence*, vol. 26, no. 10, pp. 1272–1282, 2004.

[20] H. S. Løvås, M. K. Larsen, O. Pizarro, and A. J. Sørensen, "Semi-analytical model for deep-water hyperspectral imaging," *Applied optics (2004)*, vol. 62, no. 33, pp. 8832–, 2023.

[21] B. L. McGlamery, "A computer model for underwater camera systems," in *SPIE Proceedings*, vol. 208, pp. 221–231, SPIE, 1980.

[22] L. C. Andrews and R. L. Phillips, "Prologue," in *Laser Beam Propagation through Random Media*, pp. 3–34, SPIE Press, 2005.

[23] J. R. Brownson, "Chapter 03 - laws of light," in *Solar Energy Conversion Systems* (J. R. Brownson, ed.), pp. 41–66, Boston: Academic Press, 2014.

[24] R. Jain, R. Kasturi, and B. G. Schunck, "Chapter 9 - shading," in *Machine vision*, McGraw-Hill computer science series, pp. 257–275, New York: McGraw-Hill, 1995.

[25] B. Pfrommer and K. Daniilidis, "Tagslam: Robust slam with fiducial markers," *arXiv.org*, 2019.

[26] D. Li, G. Wen, B. Wei Hui, S. Qiu, and W. Wang, "Cross-ratio invariant based line scan camera geometric calibration with static linear data," *Optics and Lasers in Engineering*, vol. 62, pp. 119–125, 2014.

[27] D. Li, W. Gongjian, and S. Qiu, "Cross-ratio–based line scan camera calibration using a planar pattern," *Optical Engineering*, vol. 55, p. 014104, 01 2016.

[28] M. A. Branch, T. F. Coleman, and Y. Li, "A subspace, interior, and conjugate gradient method for large-scale bound-constrained minimization problems," *SIAM journal on scientific computing*, vol. 21, no. 1, pp. 1–23, 1999.

[29] C. D. Mobley, H. Zhang, and K. J. Voss, "Effects of optically shallow bottoms on upwelling radiances: Bidirectional reflectance distribution function effects," *Limnology and Oceanography*, vol. 48, no. 1part2, pp. 337–345, 2003.

[30] Y. Mao, C. Betters, B. Evans, C. Artlett, S. Leon-Saval, I. Cairns, S. Garske, T. Cocks, R. Winter, and T. Dell, "OpenHSI: A novel open source hyperspectral imaging spectrometer for do-it-yourself applications," tech. rep., The University of Sydney, 2020.

[31] R. M. Pope and E. S. Fry, "Absorption spectrum (380-700 nm) of pure water. ii. integrating cavity measurements," *Applied Optics*, vol. 36, no. 33, pp. 8710–8723, 1997.